ACE-OT: Polarimetric SAR data based amplitude contrast enhancement algorithm for offset tracking applications

Sen Du, Jordi J. Mallorqui, *Senior Member, IEEE, and Feng Zhao, Member, IEEE*

***Abstract*—The use of polarimetric SAR data can improve the performance of persistent scatterer interferometry (PSI). However, its huge potential remains locked for the amplitude information based offset tracking (OT) technology. For example, to the best knowledge of the authors, there is no single example of a polarization based image optimization method that has been developed for OT processing. In this paper, an amplitude contrast enhancement algorithm (ACE) is introduced, which demonstrates the potential of the polarimetric SAR data on the improvement of OT performance. Its core idea is finding the optimal combination of the different scattering mechanisms for each pixel to improve the contrast. Firstly, the orientation of the reflected polarization ellipse is removed, to avoid the influence of the geometric relationship between the antenna and the target, and the properties of the target. Then three similarity parameters are defined to represent the three basic reflection types of the single bounce, the double bounce, and the random reflection. After that, the optimizing equation is constructed with two optimizing vectors. Finally, the optimizing vectors are calculated to obtain the enhanced amplitude image. Three examples of the enhancement are presented with different PolSAR images sets of both full- (Radarsat-2) and dual-polarization (TerraSAR-X and Sentinel-1). The performance of ACE-OT has been compared with another method, the Adaptive Histogram Enhancement (AHE). The impact of the number of polarization channels available on ACE-OT performance has also been studied.**

***Index Terms*—offset tracking, contrast enhancement, radar polarimetry, synthetic aperture radar (SAR).**

I. Introduction

DUE to its robustness for dealing with cases in which large deformations are present, amplitude image based Offset Tracking (OT) is widely used in the observation of glacier movements [1], mining caused ground deformations [2], landslides [3] and volcanic activities [4]. In these situations, traditional Persistent Scatters Interferometry (PSI), or Differential Interferometry SAR (DInSAR), methodologies are not able to deal with the strong phase decorrelation induced by large deformations.

As more SAR satellites with polarimetric capabilities are available, it is feasible to improve OT performance taking advantage of its polarimetric diversity. As one of the few OT methods using polarimetry, the polarimetric similarity tracking method was proposed to improve the accuracy of OT [1]. The multiple offset results are obtained through different polarization channels, and the hypergeometric Bessel function is applied to estimate the most likely result. This method can improve OT reliability and can be implemented into any kind of multivariate remote sensing data such as multichannel optical images. However, the polarimetric data are simply regarded as simply redundant observations, while the scattering information contained in them is not utilized. Another polarimetric data based OT method proposed by Wang defined the cross correlation according to the vector constructed by Pauli decomposition [3]. This method is able to exploit the scattering information and improve the OT accuracy, but due to the characteristics of the Pauli decomposition, the effect of the single scattering in the image is emphasized, while the effect of the volume scattering and the double scattering is being reduced. Besides, instead of doing optimization, the different kinds of reflections are simply added when calculating the correlation between two images, which does not fully exploit the potentiality of polarimetric data.

For PSI, polarimetric data based amplitude and phase optimizing methods improve the performance of deformation detection and characterization by increasing the density and quality of valid pixels with respect to the single polarization case [5]–[22]. The main idea of polarimetric optimization is to construct a polarization space and find the optimal projection of the polar vector in this space.

However, these optimization methods are not suitable for the OT case as they are based on optimizing the phase quality. Compared with the phase, the amplitude is more robust to the loss of coherence, which is the reason why OT is still a powerful alternative to DInSAR despite its lower accuracy. Therefore, this paper does not consider coherence-based phase optimization methods. For the methods where the optimization criterion is the amplitude deviation [10], [11] the information of targets at more than two different moments are required. The basic OT processing works with image pairs. Besides, the optimization methods for DInSAR assume that the offset caused by the deformation is very small, at least within one

Manuscript received **** **, ****; revised **** **, ****. This work has been financially supported by China Scholarship Council (Grant No. 201806420035); the Spanish Ministry of Science and Innovation (MCIN) and the State Research Agency (AEI) project PID2020-117303GB-C21 MCIN/AEI/10.13039/501100011033. This work has also been financially supported by Natural Science Foundation of China (Grant No. 42004011), China Postdoctoral Science Foundation (Grant No. 2020M671646), the Construction Program of Space-Air-Ground-Well Cooperative Awareness Spatial Information Project (B20046)

Sen Du and Jordi J. Mallorqui are with the CommSensLab, Universitat Politècnica de Catalunya, 08034 Barcelona, Spain (e-mail: sen.du@upc.edu; jordi.joan.mallorqui@upc.edu).

Feng Zhao is with the School of Environment Science and Spatial Informatics, China University of Mining and Technology (CUMT), Xuzhou, China and with the Key Laboratory of Land Environment and Disaster Monitoring, MNR, China University of Mining and Technology.

 DOI 10.1109/TGRS.2022.3195612

pixel. This assumption does not hold for the OT case. The offset detected by OT can be several pixels. Therefore, the existing polarimetric optimization algorithms for DInSAR are not suitable for OT.

For the amplitude information based OT, contrast is one of the most important indicators to estimate the suitability of the images. The cross-correlation between two images can not be properly calculated if distinctive features are not present. Image contrast, this is the energy distribution, is an effective quantitative indicator to measure the presence of distinctive features in a SAR image. Larger contrasts imply richer feature information. Therefore, inspired by Yang [23], [24], an amplitude optimization method based on contrast enhancement is proposed in this paper. The method improves the image contrast by searching the optimal polarization combination leading to the largest contrast according to the scattering mechanisms of ground objects, and therefore is named as Amplitude Contrast Enhancing Offset Tracking (ACE-OT).

Three different PolSAR data sets are used to assess the performance of the proposed method. One is dual-pol TerraSAR-X images over Daliuta (China), which is affected by strong mining-induced subsidence. The deformation time series are obtained by the proposed ACE-OT. The other data sets are quad-pol Radarsat-2 and dual-pol Sentinel-1 images acquired over the Barcelona airport. Because the deformation in this area is too small to be detected by OT, simulated deformations have been added to Radarsat-2 data to evaluate its performance. Sentinel-1 images are used to verify the capability of the proposed method on separating the scattering mechanisms.

The paper is organized as follows. In Section II, the proposed method is introduced. The data sets and results are described in Section III and Section IV. The discussion of the performance of different polarization channel combinations of Radarsat-2 and Sentinel-1 is performed in Section V. Finally, conclusions are given in Section VI.

II. Methodology

The overall scheme of the proposed method is shown in Fig. 1(a). Similar to the conventional OT, images need to be co-registered and base-banded before their interpolation and cross correlation calculation. The scheme of the amplitude enhancement method is shown in Fig. 1(b). The step marked with a dotted line can only be applied to quad-pol data.

Instead of only enhancing part of the image [23], the proposed method can improve the contrast of the whole image. In the particular case of a monostatic system, as the sensors considered in this paper, the cross-polar channels should be equal, i.e. $S_{HV} = S_{VH}$.

The enhancement algorithm is mainly composed of three steps: orientation elimination, similarity parameter acquisition and contrast optimization.

A. Orientation elimination

The complex back scattering matrix $\mathbf{S}$ for a monostatic radar can be defined as [25]–[28]:

$$[\mathbf{S}] = \begin{bmatrix} S_{HH} & S_{HV} \\ S_{VH} & S_{VV} \end{bmatrix} \quad (S_{HV} = S_{VH}) \tag{1}$$

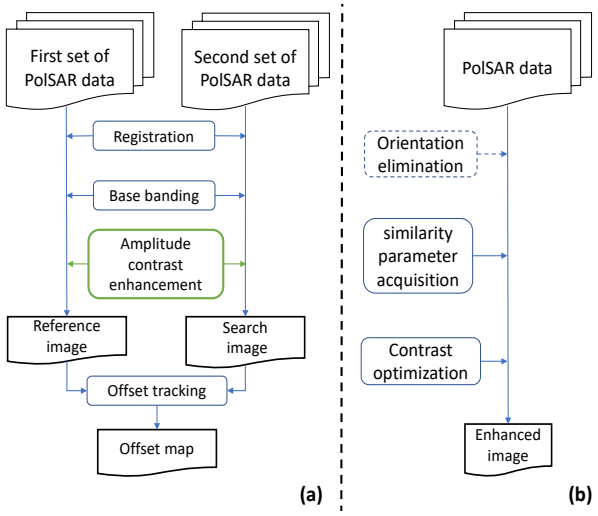

Fig. 1. Scheme of the proposed ACE-OT. (a) Overall scheme of the OT process. (b) Sub-scheme of the Amplitude Contrast Enhancement procedure.

where S_{HH}, S_{HV}, S_{VH}, S_{VV} are the different polarimetric channels of the target response. The subscript means the polarization of the received and transmitted signals.

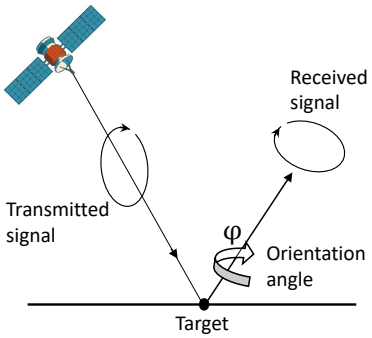

Fig. 2. Polarization ellipse rotation of the target reflection with respect the transmitted one.

It can be seen from Fig. 2 that after the reflection, the polarization ellipse of the received signal is rotated by an angle φ with respect to the transmitted one. The angle φ depends on the geometric relationship between the antenna and the target, and the properties of the target. Scattering matrices of some targets are orientation independent, while others are not [29]. The ellipse orientation could change the phase information in the received signals, it is thus necessary to eliminate it with Eq. (2)

$$[\mathbf{S}^0] = [\mathbf{J}(-\varphi)] \cdot [\mathbf{S}] \cdot [\mathbf{J}(\varphi)] = \begin{bmatrix} S^0_{HH} & S^0_{HV} \\ S^0_{VH} & S^0_{VV} \end{bmatrix} \tag{2}$$

where

$$[\mathbf{J}(\varphi)] = \begin{bmatrix} \cos\varphi & -\sin\varphi \\ \sin\varphi & \cos\varphi \end{bmatrix} \tag{3}$$

the orientation φ can be obtained by the Huynen decomposition [29]

$$\varphi = \frac{1}{2} \cdot \arctan \frac{2 \cdot \mathrm{Re}\left\{S^*_{HV}\left(S_{HH} + S_{VV}\right)\right\}}{\left|S_{HH} - S_{VV}\right|^2} \tag{4}$$

where Re means retaining the real part of a complex number and $*$ means complex conjugate.

After the operation by Eq. (2), (3) and (4), the influence of the ellipse orientation on the following calculations can be avoided. This step can not be applied to dual-pol data as the orientation φ can not be determined with Eq. (4).

B. Similarity parameters acquisition

The proposed method defines three similarity parameters according to [23]. The first two parameters r_1 and r_2 describe two basic scattering mechanisms: single reflection and double reflection from a target, as shown in Eq. (5) and (6). r_1 is large in calm sea areas or smooth surfaces like roads, roofs or fields. r_2 is small in the previous cases but large in urbanized areas. The third parameter, r_3, is the polarization entropy [30], which is very good for measuring the randomness of targets like those affected by volume scattering, shown in Eq. (7).

$$r_1 = \frac{\left|S^0_{HH} + S^0_{VV}\right|^2}{2\left(\left|S^0_{HH}\right|^2 + \left|S^0_{VV}\right|^2 + 2\left|S^0_{HV}\right|^2\right)} \tag{5}$$

$$r_2 = \frac{\left|S^0_{HH} - S^0_{VV}\right|^2}{2\left(\left|S^0_{HH}\right|^2 + \left|S^0_{VV}\right|^2 + 2\left|S^0_{HV}\right|^2\right)} \tag{6}$$

$$r_3 = -\sum_{i=1}^{3} P_i \log_3 P_i \tag{7}$$

$$P_i = \frac{\lambda_i}{\sum_{k=1}^{3}\lambda_k}, \quad \sum_{k=1}^{3} P_k = 1 \tag{8}$$

$$\mathbf{k}_T = \frac{1}{\sqrt{2}}\begin{bmatrix} S^0_{HH} + S^0_{VV} \\ S^0_{HH} - S^0_{VV} \\ 2S^0_{HV} \end{bmatrix} \tag{9}$$

$$\mathbf{T} = \frac{1}{L}\sum_{n=1}^{L}(\mathbf{k}_T \cdot \mathbf{k}_T^+) \tag{10}$$

r_3 can be obtained by Eq. (7), (8), (9) and (10). Where $\mathbf{k}_T$ is the Pauli spin matrix, λ_i the eigenvalues of the polarization coherence matrix $\mathbf{T}$ by singular value decomposition, P_i the pseudo probability obtained from the eigenvalues, L the number of looks, and $+$ the Hermitian or conjugate transpose. In this paper, $\mathbf{T}$ is calculated with a 3×3 averaging window.

The values of r_1, r_2 and r_3 range from 0 to 1. The larger the parameter, the stronger the corresponding reflection type. For example, a large r_1 value represents that the reflection is mainly a single bounce.

C. Contrast optimization for quad-pol data

The optimization of the polarimetric contrast enhancement (OPCE) can increase the contrast between two kinds of targets [28], [31], [32]. Assuming $\mathbf{T}_\mathrm{A}$ and $\mathbf{T}_\mathrm{B}$ are the average scattering matrices of two ground targets, $\bar{\mathbf{K}}(\mathbf{T}_\mathrm{A})$ and $\bar{\mathbf{K}}(\mathbf{T}_\mathrm{B})$ are their Kennaugh matrices. The Kennaugh matrix can be obtained according to,

$$\bar{\mathbf{K}} = \left\langle \mathbf{A}_4^* \left([\mathbf{S}^0] \otimes [\mathbf{S}^0]^*\right) \mathbf{A}_4^{-1} \right\rangle \tag{11}$$

where $\otimes$ represents the tensor product and $\mathbf{A}_4$ is,

$$\mathbf{A}_4 = \begin{bmatrix} 1 & 0 & 0 & 1 \\ 1 & 0 & 0 & -1 \\ 0 & 1 & 1 & 0 \\ 0 & j & -j & 0 \end{bmatrix} \tag{12}$$

The OPCE optimization consists on finding $\mathbf{g} = (1, g_1, g_2, g_3)^t$ and $\mathbf{h} = (1, h_1, h_2, h_3)^t$ that maximizes the power ratio of $\mathbf{T}_\mathrm{A}$ and $\mathbf{T}_\mathrm{B}$ with constrains, i.e.,

$$\begin{aligned} \text{maximize} \quad & \frac{\mathbf{h}^t[\bar{\mathbf{K}}(\mathbf{T}_\mathrm{A})]\mathbf{g}}{\mathbf{h}^t[\bar{\mathbf{K}}(\mathbf{T}_\mathrm{B})]\mathbf{g}} \\ \text{subject to} \quad & g_1^2 + g_2^2 + g_3^2 = 1 \\ & h_1^2 + h_2^2 + h_3^2 = 1. \end{aligned} \tag{13}$$

Yang. [23] assumed that the optimal function should contain the scattering characteristics of the target. However, under normal circumstances, we cannot know the optimal functional form. Therefore, GOPCE assumes that the functional form includes two factors. One factor is the received energy, which is mentioned in OPCE, and the other is the scattering characteristics of the target. Same as $\mathbf{h}$ and $\mathbf{g}$, $\mathbf{x}$ helps find the maximum power ratio of $\mathbf{T}_\mathrm{A}$ and $\mathbf{T}_\mathrm{B}$.

$$\begin{aligned} \text{maximize} \quad & \frac{\frac{1}{M}\sum_{\mathbf{T}_\mathrm{A}}\left[\sum_{i=1}^{3} x_i r_i(\mathbf{T}_\mathrm{A})\right]^2}{\frac{1}{N}\sum_{\mathbf{T}_\mathrm{B}}\left[\sum_{i=1}^{3} x_i r_i(\mathbf{T}_\mathrm{B})\right]^2} \times \frac{\mathbf{h}^t[\bar{\mathbf{K}}(\mathbf{T}_\mathrm{A})]\mathbf{g}}{\mathbf{h}^t[\bar{\mathbf{K}}(\mathbf{T}_\mathrm{B})]\mathbf{g}} \\ \text{subject to} \quad & g_1^2 + g_2^2 + g_3^2 = 1 \\ & h_1^2 + h_2^2 + h_3^2 = 1 \\ & x_1^2 + x_2^2 + x_3^2 = 1 \end{aligned} \tag{14}$$

where M and N denote the selected pixel numbers of $\mathbf{T}_\mathrm{A}$ and $\mathbf{T}_\mathrm{B}$, respectively. It can be seen from Eq. (14) that the contrast can be improved by enhancing the desired target $\mathbf{T}_\mathrm{A}$ versus the undesired target $\mathbf{T}_\mathrm{B}$.

For the OT applications, the contrast of the whole image needs to be enhanced instead of only two kinds of targets. The contrast calculation proposed by Cumming [33] can be applied as the optimizing criteria:

$$C = \frac{E\left(|I|^2\right)}{[E(|I|)]^2} \tag{15}$$

where I is intensity and E the mathematical expectation. To obtain the maximum contrast, the optimal equation is established according to GOPCE.

$$\begin{aligned} \mathrm{OP} = & \left[\sum_{i=1}^{3} x_i r_i\right]^2 \times \mathbf{h}_m^t[K]\mathbf{g}_m \\ \text{subject to} \quad & \mathbf{g} = (1, g_1, g_2, g_3)^t \\ & \mathbf{h} = (1, h_1, h_2, h_3)^t \\ & \mathbf{x} = (x_1, x_2, x_3)^t \\ & g_1^2 + g_2^2 + g_3^2 = 1 \\ & h_1^2 + h_2^2 + h_3^2 = 1 \\ & x_1^2 + x_2^2 + x_3^2 = 1 \end{aligned} \tag{16}$$

The optimal polarization states $\mathbf{g}$, $\mathbf{h}$, and $\mathbf{x}$ are the same as those of the GOPCE. The maximum contrast can be achieved

after finding these optimal states. From Eq. (16) it is known that $\mathbf{g}$, $\mathbf{h}$, and $\mathbf{x}$ could be the coordinates of a point that is on a spherical surface with a radius of 1 and centered at the origin of coordinates, $(0,0,0)$. Therefore, the original 9 parameters to be optimized can be reduced to 6, i.e.,

$$\begin{aligned}\mathbf{g} &= (1, \sin\alpha\cos\theta, \sin\alpha\sin\theta, \cos\alpha)^t \\ \mathbf{h} &= (1, \sin\beta\cos\gamma, \sin\beta\sin\gamma, \cos\beta)^t \\ \mathbf{x} &= (1, \sin\delta\cos\epsilon, \sin\delta\sin\epsilon, \cos\delta)^t\end{aligned} \tag{17}$$

For a multi-parameter optimization problem, many approaches can be applied, such as the Newton-Raphson method, quasi Newton method, and the Conjugate Gradient Method (CGM). Due to its low computational burden and high computational efficiency, CGM [34] is applied to obtain $\mathbf{g}$, $\mathbf{h}$, and $\mathbf{x}$ for maximizing the contrast in Eq. (15). The enhanced amplitude image can be generated once the parameters $\mathbf{g}$, $\mathbf{h}$, and $\mathbf{x}$ are obtained.

D. Contrast optimization for dual-pol data

Since dual-pol SAR is quite common as some polarimetric sensors can not provide quad-pol data, like Sentinel-1, it is necessary to consider their capabilities for contrast enhancement. There are two kinds of combinations for dual-pol data: two co-polar channels (i.e., $\{HH, VV\}$) and a co-polar and a cross-polar channels (i.e., $\{HH, VH\}$ or $\{VV, HV\}$). As the processing and the behaviour of the enhancement strongly depends on the presence of a cross-polar channel, they will be presented separately.

1) Enhancement with $\{HH, VV\}$: The lack of cross-pol data makes impossible to eliminate the orientation. Consequently, the contrast enhancement starts with the calculation of the similarity parameters. r_1, r_2 and r_3 are defined as:

$$r_1 = \frac{|S_{HH} + S_{VV}|^2}{2\left(|S_{HH}|^2 + |S_{VV}|^2\right)} \tag{18}$$

$$r_2 = \frac{|S_{HH} - S_{VV}|^2}{2\left(|S_{HH}|^2 + |S_{VV}|^2\right)} \tag{19}$$

$$r_3 = -\sum_{i=1}^{2} P_i \log_2 P_i \tag{20}$$

As in the quad-pol case, r_3 is calculated by the pseudo probabilities obtained from the eigenvalues of the polarization coherence matrix $\mathbf{T}$. From Eq. (21) it is known that due to the lack of the cross-pol data, $\mathbf{k}_T$ becomes a two-dimensional vector, $\mathbf{T}$ thus turns into a 2×2 matrix. Therefore, only two eigenvalues can be obtained, instead of the three of quad-pol data, and the pseudo probabilities are calculated with Eq. (22)

$$\mathbf{k}_T = \frac{1}{\sqrt{2}} \begin{bmatrix} S_{HH} + S_{VV} \\ S_{HH} - S_{VV} \end{bmatrix} \tag{21}$$

$$P_i = \frac{\lambda_i}{\sum_{k=1}^{2} \lambda_k}, \quad \sum_{k=1}^{2} P_k = 1 \tag{22}$$

Although values for r_3 can be obtained, the absence of cross-pol data make them potentially inaccurate and noisy. The entropy maps obtained from $HH - VV$ data are compared with those obtained with quad-pol data. Sections IV-B and Section V show and discuss the results. Therefore, this lack of reliability of r_3 forces it to do not allow its participation in the contrast enhancement.

The scattering matrix in this case becomes:

$$[\mathbf{S}] = \begin{bmatrix} S_{HH} & 0 \\ 0 & S_{VV} \end{bmatrix} \tag{23}$$

With $\mathbf{S}$ the Kennaugh matrix $[\mathbf{K}]$ can be obtained. The optimization equation is defined as:

$$\begin{aligned} \text{OP} &= \left[\sum_{i=1}^{2} x_i r_i\right]^2 \times \mathbf{h}_m^t [\mathbf{K}] \mathbf{g}_m \\ \text{subject to} \quad & \mathbf{g} = (1, g_1, g_2, g_3)^t \\ & \mathbf{h} = (1, h_1, h_2, h_3)^t \\ & \mathbf{x} = (x_1, x_2)^t \\ & g_1^2 + g_2^2 + g_3^2 = 1 \\ & h_1^2 + h_2^2 + h_3^2 = 1 \\ & x_1^2 + x_2^2 = 1 \end{aligned} \tag{24}$$

Once the optimized equation is established, CGM is used to find $\mathbf{g}$, $\mathbf{h}$, and $\mathbf{x}$ that maximize the contrast.

2) Enhancement with $\{HH, VH\}$ or $\{VV, HV\}$: As there is only one co-polar channel, xx, r_1 and r_2 will be identical. Therefore, only r_1 and r_3 participate in the contrast enhancement. They are defined as:

$$r_1 = \frac{|S_{\text{xx}}|^2}{2\left(|S_{\text{xx}}|^2 + 2\,|S_{HV}|^2\right)} \tag{25}$$

$$r_3 = -\sum_{i=1}^{2} P_i \log_2 P_i \tag{26}$$

$$P_i = \frac{\lambda_i}{\sum_{k=1}^{2} \lambda_k}, \quad \sum_{k=1}^{2} P_k = 1 \tag{27}$$

$$\mathbf{k}_T = \frac{1}{\sqrt{2}} \begin{bmatrix} S_{\text{xx}} \\ 2S_{HV} \end{bmatrix} \tag{28}$$

The scattering matrix becomes:

$$[\mathbf{S}] = \begin{bmatrix} S_{HH} & S_{HV} \\ S_{HV} & 0 \end{bmatrix} \text{ or } \quad [\mathbf{S}] = \begin{bmatrix} 0 & S_{HV} \\ S_{HV} & S_{VV} \end{bmatrix} \tag{29}$$

With $\mathbf{S}$ the Kennaugh matrix, $[\mathbf{K}]$ can be obtained. The optimization equation is defined as:

$$\begin{aligned} \text{OP} &= (x_1 r_1 + x_3 r_3)^2 \times \mathbf{h}_m^t [K] \mathbf{g}_m \\ \text{subject to} \quad & \mathbf{g} = (1, g_1, g_2, g_3)^t \\ & \mathbf{h} = (1, h_1, h_2, h_3)^t \\ & \mathbf{x} = (x_1, x_3)^t \\ & g_1^2 + g_2^2 + g_3^2 = 1 \\ & h_1^2 + h_2^2 + h_3^2 = 1 \\ & x_1^2 + x_3^2 = 1 \end{aligned} \tag{30}$$

III. Test sites and Data sets

To validate the proposed amplitude contrast enhancement method, two different scenarios (an airport and a mountainous area) and three SAR data sets have been selected. The first one consists of 31 stripmap quad-pol Radarsat-2 images over the Barcelona airport (Spain), acquired from June 2010 to July 2012. The resolution is 5.1 m in azimuth and 4.7 m in range. Since the real deformation is too small to be detected by OT, simulated offsets have been added to the images. Over the same scenario, 32 dual-pol $\{VV, HV\}$ Sentinel-1 A/B images acquired from 2 April, 2018 to 5 October, 2018, have also been processed. In its Interferometric Wide Swath (IW) mode features a spatial resolution ranging from 2.7 to 3.5 m in range and 22.0 m in azimuth with a 250 km swath. Both sensors work at C-band.

The last test site is located in Daliuta (China), a mountainous area affected by large ground deformations caused by coal mining activities. The data set covering this area consists of 20 TerraSAR-X SPOT dual-pol images $\{HH, VV\}$, acquired from April 2014 to December 2014, with a resolution of 2.2 m in azimuth and 1.2 m in range. TerraSAR-X works at X-band and has a revisit period of 11 days.

Besides the PolSAR images, SRTM DEMs with a resolution of 90 m have been used to help with the images' co-registration [35].

IV. Results

A. Results of quad-pol Radarsat-2 images

Because the proposed method performs contrast enhancement based on the scattering mechanism of the ground targets, it is very important whether the scattering types are correctly retrieved. Fig. 3 shows the reflection types in the airport area, calculated from the temporal average of the 31 Radarsat-2 images, as well as the optical image to help recognize ground features. As expected, the value of r_1 is large in airport runways, sea, bare land, and roofs of large buildings, r_2 is large in urbanized areas and r_3 is large in vegetated areas and areas with complex structures that induce volume scattering, such as the airport terminal.

Four typical ground features (farmland with vegetation, roads, sea and buildings) are selected to analyze their scattering characteristics. Their locations are marked with orange, magenta, and blue rectangles in Fig. 3(a). The scatter plots between the three similarity parameters and the amplitude are shown in Fig. 4. The average amplitudes of the two co-polar and one cross-polar channels are used as the abscissa for all cases. It can be seen that the four features present different amplitude distributions. The sea area and roads have the largest concentration of low amplitudes as they reflect less energy. Their scattering is single-bounce. On the contrary, the buildings have higher and more disperse amplitude values due to their complex structures. Their scattering is mostly double-bounce.

From Fig. 4, one easily finds that the largest values of r_1 are associated to sea area and roads, of r_2 to buildings and of r_3 to farm. The scattering characteristics of the four ground features in Fig. 4 are consistent with the results in Fig. 3, which means r_1, r_2 and r_3 can represent the single, double and random reflection, respectively.

After the validation of the scattering mechanism separation, the amplitude contrast enhancement is applied to Radarsat-2 images and the result is shown in Fig. 5.

There are many methods to enhance image contrast, but as far as the authors know, they are based on pure image processing and they do not consider or take advantage of the scattering mechanisms information present in the data. A classical method called Adaptive Histogram Equalization (AHE) has been selected to compare with the proposed method [36]. AHE involves applying contrast enhancement based on the local region surrounding each pixel. Each pixel is mapped to an intensity proportional to its rank within the surrounding neighborhood. This method of automatic contrast enhancement has proven to be broadly applicable to a wide range of images and have demonstrated its effectiveness. It has been selected for comparison purposes as it works locally, as ACE.

The contrast of each polarimetric channel is around 1.25, the contrast of their average amplitudes image is 1.12, while the AHE and ACE contrast are 1.74 (over the averaged amplitude image) and 2.76, respectively. Fig, 6 shows the amplitude distributions for each case. AHE only changes the amplitude values from the original Rayleigh distribution to a uniform one, with no consideration of the scattering mechanisms. It can be seen that the airport runways and the sea area are brighter after AHE, although the received energy from these areas was small, making the data noisier. On the contrary, with ACE the areas with strong scatters are emphasized, such as the airport terminals and buildings, while the weak areas are emaciated, such as the airport runways, the roads and swamp in the bottom of the image. From the amplitude image and the three scatter mechanism maps we can see that there are many speckles in the farmland and some roads. These speckles can be associated to small towers, small bridges, small piers or even rocks which are highlighted by ACE, although they can also be noise in some cases. Generally speaking, the enhancement of all the distinctive features present in the images contribute to the contrast improvement.

The cross correlations of the amplitude images with and without the enhancements are calculated and shown in Fig. 7. The images were acquired on January 15, 2011, and July 2, 2011. Fig. 7(a) shows the cross correlation calculated by the average amplitude of the original HH, VV, and HV polarization data, and Fig. 7(b) and (c) show the cross correlation of the images enhanced by AHE and ACE respectively. It can be seen that after AHE, the gradient near the peak of correlation is larger, which is beneficial for offset tracking. However, the cross correlation coefficient also increase for almost the whole map, meaning that the two amplitude images, although having larger contrast, become more different after the enhancement. This can be attributed to the contrast enhancement in areas with random behaviours, like the sea, or low signal, like runaways. In the case of ACE, the cross correlation peak is sharper and the gradient near the peak is increased, while the cross correlation coefficient decreases elsewhere.

To demonstrate the advantage of the enhancement method, an OT processing is carried out with the same two images. A

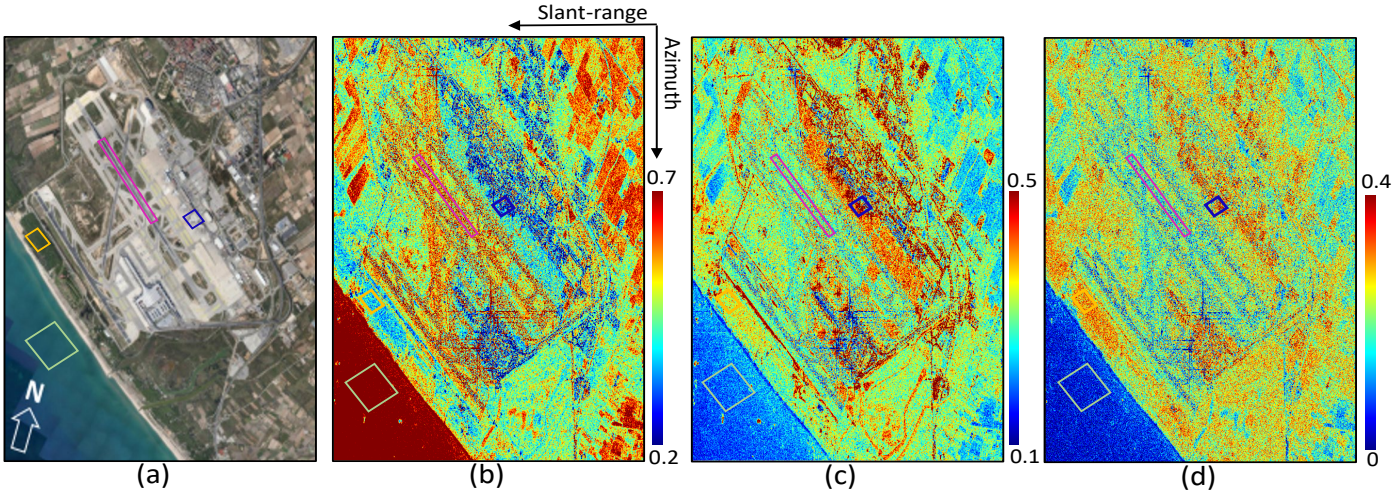

Fig. 3. Temporal average scatter mechanism maps obtained from quad-pol Radarsat-2 images with the coverage size of 4600m × 2829m. (a) Optical image from Google Earth. (b) Value of similarity parameter r_1, related to the measurement of single reflections. (c) Value of similarity parameter r_2, related to the measurement of double reflections. (d) Value of similarity parameter r_3, i.e., polarization entropy, related to the measurement of randomness. The features highlighted with orange, magenta, green and blue rectangles in (a) are a farmland with vegetation, a road, sea area and a building, respectively.

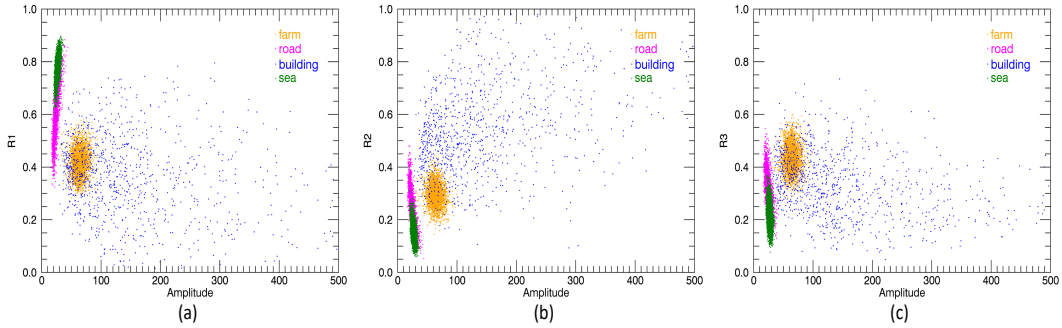

Fig. 4. Relationship between amplitude and similarity parameters of different ground features. Scatter plots of similarity parameters vs amplitude (a) r_1, (b) r_2 and (c) r_3.

simulated offset in slant range direction is added on the second one as the real deformation is extremely weak. The template size is set to 64×64 pixels with no windowing. The simulated offset, and the offset obtained with the original images and the images enhanced by AHE and ACE are shown in Fig. 8(a), (b), (c) and (d) respectively. It can be seen that the shape of the offset area in (b), (c) and (d) are similar to the simulated one, while it is clear that the result of ACE enhanced images is smoother and has fewer abnormal values. Non-realistic offsets are obtained in the lower left corners of Fig. (b),(c) and (d), which belong to the sea. In an operational use of the method, the sea should be masked. Another wrong result is located in the area highlighted with the red circle in Fig. 8(d) that is caused by dramatic seasonal changes on the amplitude. It is obvious from (d)-(f) that vegetation has disappeared in winter and grew up again in summer.

A simulated time dependant deformation is added to the 31 Radarsat-2 images mentioned in Section III. The deformation rate is set to be linear. After the image enhancement and masking of the sea and error prone areas, OT is applied with a template size of 64×64 pixels. The deformation time series are obtained and shown in Fig. 9. The image pair used corresponds to the deformation period indicated at the bottom of each deformation map. For each time span, the first column shows the simulated offset. The second is the offset obtained with averaged images while the third is the error (the difference between the retrieved deformation values and the real ones). The fourth is the offset obtained with images enhanced by AHE, and the fifth is the error. Finally, the sixth ad seventh are the results with the images enhanced by ACE. Deformation maps have color-scales ranging from -2 to +2 pixels while error maps from -0.5 to +0.5 pixels. Results for eight different periods are shown. The template size has a direct impact on the capability of OT to monitor non-spatially uniform deformations. These estimation errors are more noticeable in areas with larger deformation gradients, like the boundaries of the deformation bowl. Due to the averaging effect, some bias in the results can be found in areas with non-uniform deformation. The best results are obtained with ACE, no artifacts can be found outside the deformation bowl and the shape and values of deformation are determined with an acceptable degree of precision, around ± 0.2 pixels, for an OT estimation. The results with the original averaged images present artifacts outside the deformation bowl and their shape and values are not as precise as with ACE. Finally, AHE results are not satisfactory as well. The shape of the

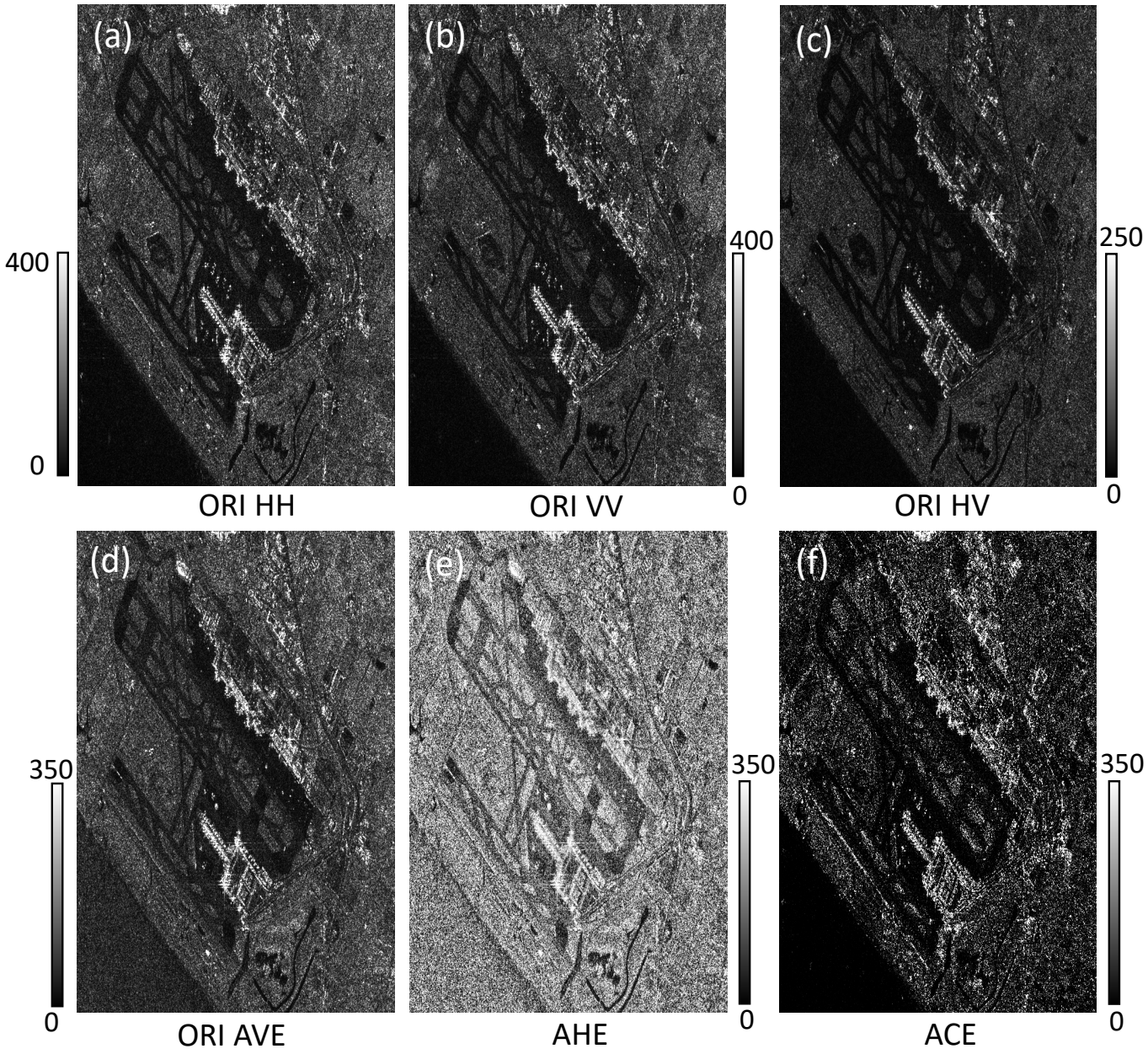

Fig. 5. Amplitude comparison before and after the application of the two contrast enhancements. The images are acquired on January 20, 2010. (a), (b) and (c) show the original HH, VV and HV amplitudes (the file values no-radiometrically corrected), respectively. (d) is the averaged amplitude from the four polarimetric channels, (e) is the AHE contrast enhanced amplitude, (f) is the ACE contrast enhanced amplitude. (d), (e) and (f) use identical scale bars for a better comparison.

deformation bowl is worsely estimated and the error values present a larger deviation.

The histograms of the error of the last time-span of Fig. 9 - 20100613-20120626 are shown in Fig. 10. It can be observed that the error distribution is not symmetric and biased to positive values. As expected, the ACE error histogram is the one that presents the lower dispersion, followed by the original averaged images and, closely, by AHE. The mean error for each case is -0.002, 0.076 and 0.008 with error standard deviations of 0.073. 0.155 and 0.214, respectively. Clearly, ACE is the method that provides the best results while AHE has the largest standard deviation of all.

B. Results of dual-pol TerraSAR-X images

The temporal average scattering mechanism decomposition results of mountainous area in Daliuta with 20 dual-pol $\{HH, VV\}$ TerraSAR-X images are shown in Fig. 11. Single reflections mainly happen on roads, farmlands with no vegetation, and valley flat areas. Double reflections distribute in hillsides, ridges, and building areas. The acquired entropy is noisy and inaccurate due to the lack of cross-polar data. This is the reason that entropy does not participate in the enhancement processing for the $\{HH, VV\}$ case.

Same as in the airport test site, the scatter plots between the similarity parameters of the three typical ground features

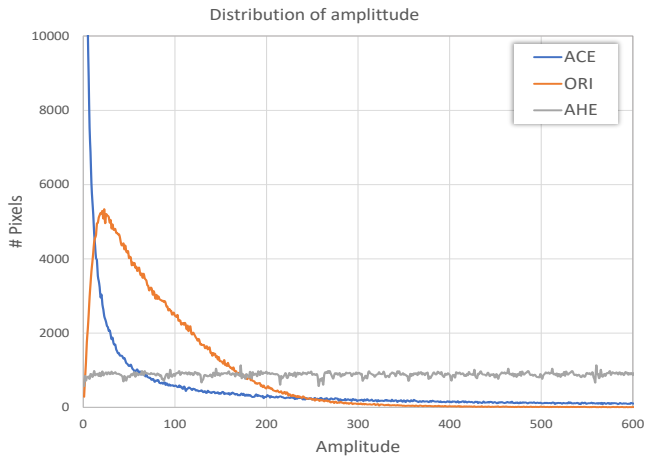

Fig. 6. Amplitude distribution for the original averaged polarimetric channels and the contrast optimized with AHE and ACE images.

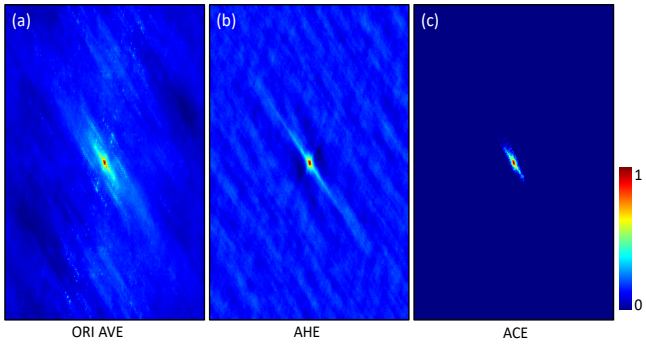

Fig. 7. Cross correlation comparison before and after contrast enhancements with January 15, 2011 and July 2, 2011 images. (a) is the cross-correlation obtained from the average amplitudes of the original HH, VV and HV channels, (b) and (c) are the cross-correlation maps obtained from the images enhanced with AHE and ACE, respectively.

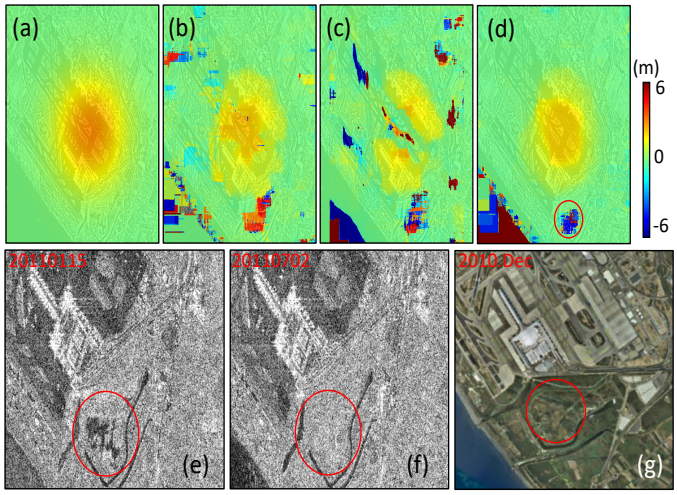

Fig. 8. OT result. (a) is the simulated deformation in slant-range, (b) the deformation obtained with the original averaged channels, (c) and (d) the deformation obtained with images enhanced with AHE and ACE, respectively. (e) and (f) are a detailed view of the HH channel amplitude acquired on January 15, 2011 and July 2, 2011, respectively. (g) is the optical image of the same area from Google Earth. The red circle in (d) highlights a swamp that causes a strong variation of the amplitude in the temporal time-span.

(farmland, road and building) and the average amplitude are shown in Fig. 12. Compared with the farmland in the airport test site, the vegetation in the mountainous area is sparser and its height is lower, therefore the reflection is mainly single bounce. Although the amplitude difference between the three typical ground features in mountainous areas is small, it can still be seen that the group separation is clear in Figure (a) and (b). The lack of cross-polarization data leads to the confusion of different features about entropy.

It can be seen in Fig. 13 that the averaging does not improves the contrast. AHE and ACE make the building in the middle of the image sharper. On the other side, the road is highlighted with ACE. Overall, the optimization effect is not as significant as in the airport test site due to the lack of cross-pol data. In addition, the contrast of the original data in the mountainous area is not as high as in the airport case.

After the enhancement, OT is applied to detect the deformation caused by coal mining. SAR images are base-banded before OT to accommodate the azimuth-varying spectra inherent to the spotlight mode and perform an alias-free interpolation. The size of the search window is set to 64×64 pixels to ensure a narrow correlation peak while retaining the deformation resolution.

The oversampling factor is set to 64 prior to cross correlation to reduce bias errors and noise [37]. The offset is converted, assuming that deformation is vertical, into subsidence, S_{sub}, with,

$$S_{\text{sub}} = \frac{P_{\text{offset}} \cdot R_{\text{size}}}{\cos\theta} \tag{31}$$

Where P_{offset} is the measured offset in pixels before and after the deformation in the slant-range direction, θ is the local incident angle and R_{size} the pixel size in the range direction. The assumption that the deformation is vertical is realistic as the horizontal movement caused by underground mining is usually very small, about one-tenth of the vertical deformation [2].

Fig. 14 shows the deformation time-series. The image pairs are the same as the deformation period indicated at the bottom of each deformation map. The first two rows are the result obtained with averaged images. The middle two rows and the last two rows are obtained with images enhanced by AHE and ACE, respectively. The deformation trends of the three approaches are similar, although the results with the first two are noisier and with more artifacts outside the deformation bowl. It can be seen from the results that the deformation area was growing to the right during the entire observation period and can be divided into two parts. The first sinking area resembles a triangle as a whole and was formed from April 5, 2014 to May 19, 2014. The subsidence values in this area are relatively large, reaching a maximum value close to 4 m. The second sinking area is strip-shaped and began to develop on May 19, 2014 and reached its maximum in early July 2014. After that, the deformation bowl remained basically unchanged, but the sinking values continued to increase. The shape and development of the second sinking area are the typical underground-mining caused deformation. The coal seams in this area are thick and shallow. Therefore, it

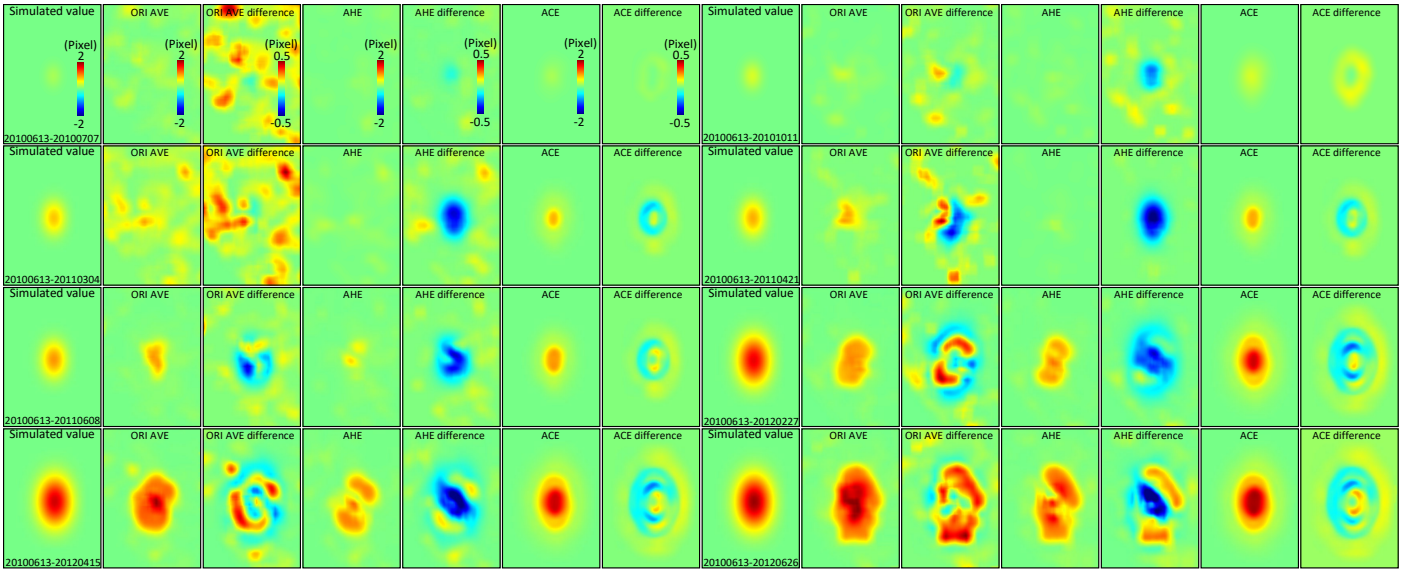

Fig. 9. Simulated deformation time-series using Radarsat-2 data. There are 8 different time spans. For each one 7 images are shown: the simulated slant-range deformation, the deformation obtained from the averaged polarimetric channels and its error, deformation obtained with AHE enhanced images and its error map, and, finally, deformation obtained with ACE enhancement and its error map.

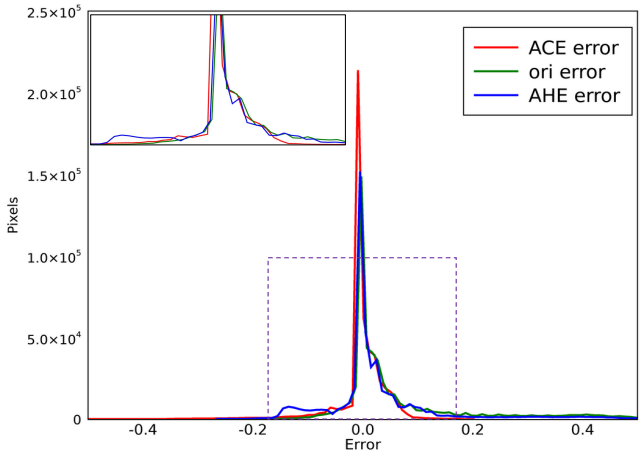

Fig. 10. Error distributions for each of the three evaluated methods for the pair with the largest time-span, 20100613-20120626 (yyyymmdd).

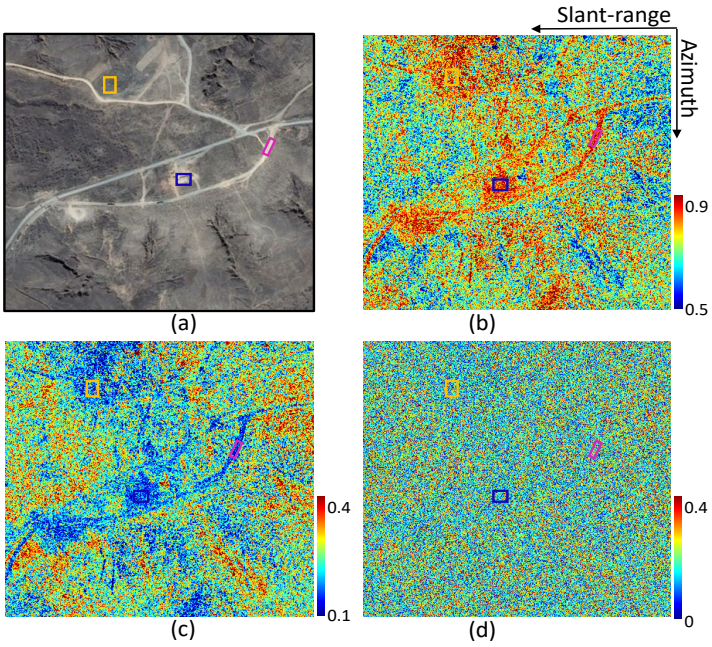

Fig. 11. Scatter mechanism maps derived from the averaged dual-pol polarimetric channels of TerraSAR-X dataset with the coverage size of 878m $\times$ 451m. (a) Optical image from Google Earth. (b), (c) and (d) are the values of similarity parameters r_1, r_2 and r_3. The features highlighted with in orange, magenta and blue rectangles in are a farmland, a road and a building, respectively.

is speculated that the first sinking area was caused by mining at the same working face but the surface collapsed, resulting in drastic changes in deformation and irregular shapes at the beginning of the observation.

C. Results of dual-pol Sentinel-1 images

Sentinel-1 images are nowadays one of the most widely used dual-pol SAR data. In its Interferometric Wide Swath (IW) mode, which is the main operational mode over land, offers dual-pol data products. The performance of ACE with this sensor has been evaluated with the comparison of the same pol combination of Radarsat-2 data. The temporal average scattering mechanism decomposition results in the same area covered by Radarsat-2 data are obtained with 32 dual-pol $\{VV, HV\}$ Sentinel-1 A/B images acquired from 2 April, 2018 to 5 October, 2018, and shown in Fig. 15. As with the processing of Radarsat-2 images, no multi-look has been done and an averaging window of 3×3 has been applied. It can be seen in Fig. 15 (a) and (c) that r_1 obtained with Sentinel-1 data is quite similar with that obtained with Radarsat-2.

For example, buildings in black circles 1 and 2 have large r_1 values, the vegetated area in black circle 4 has low r_1 values, and the bare lands in black circles 3 and 5 have higher r_1

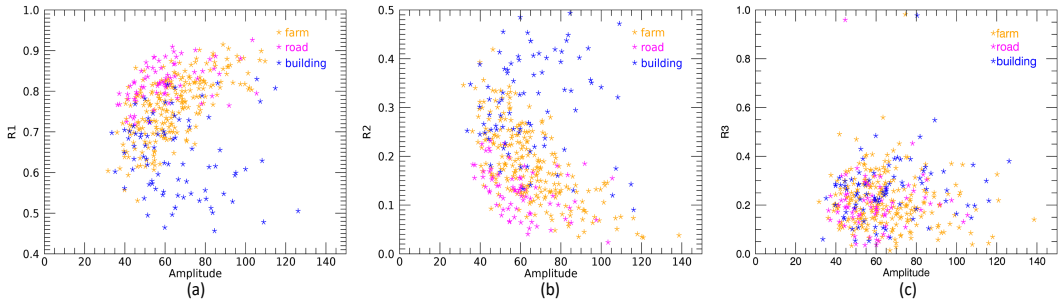

Fig. 12. Scatter plots of similarity parameters vs amplitude for different ground features: (a) r_1,(b) r_2 and (c) r_3.

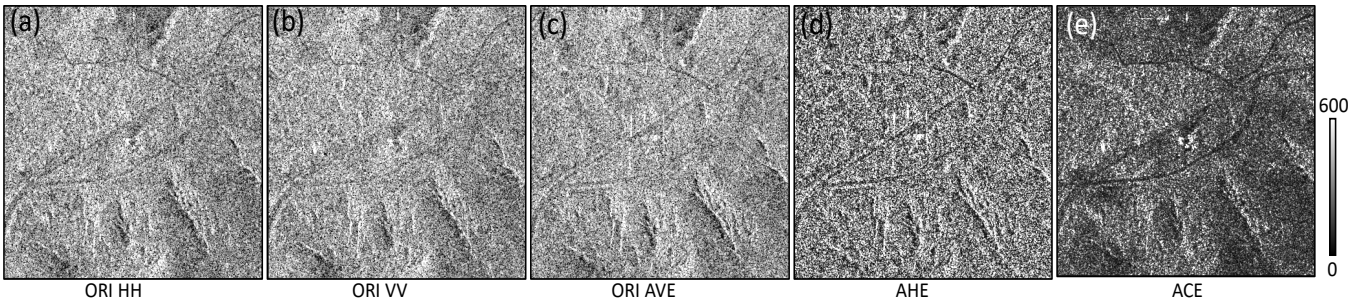

Fig. 13. Amplitude comparison before and after the contrast enhancement. (a) and (b) are the original HH and VV channels. (c) is the averaged channels. (d) and (e) are the contrast enhanced images by AHE and ACE, respectively.

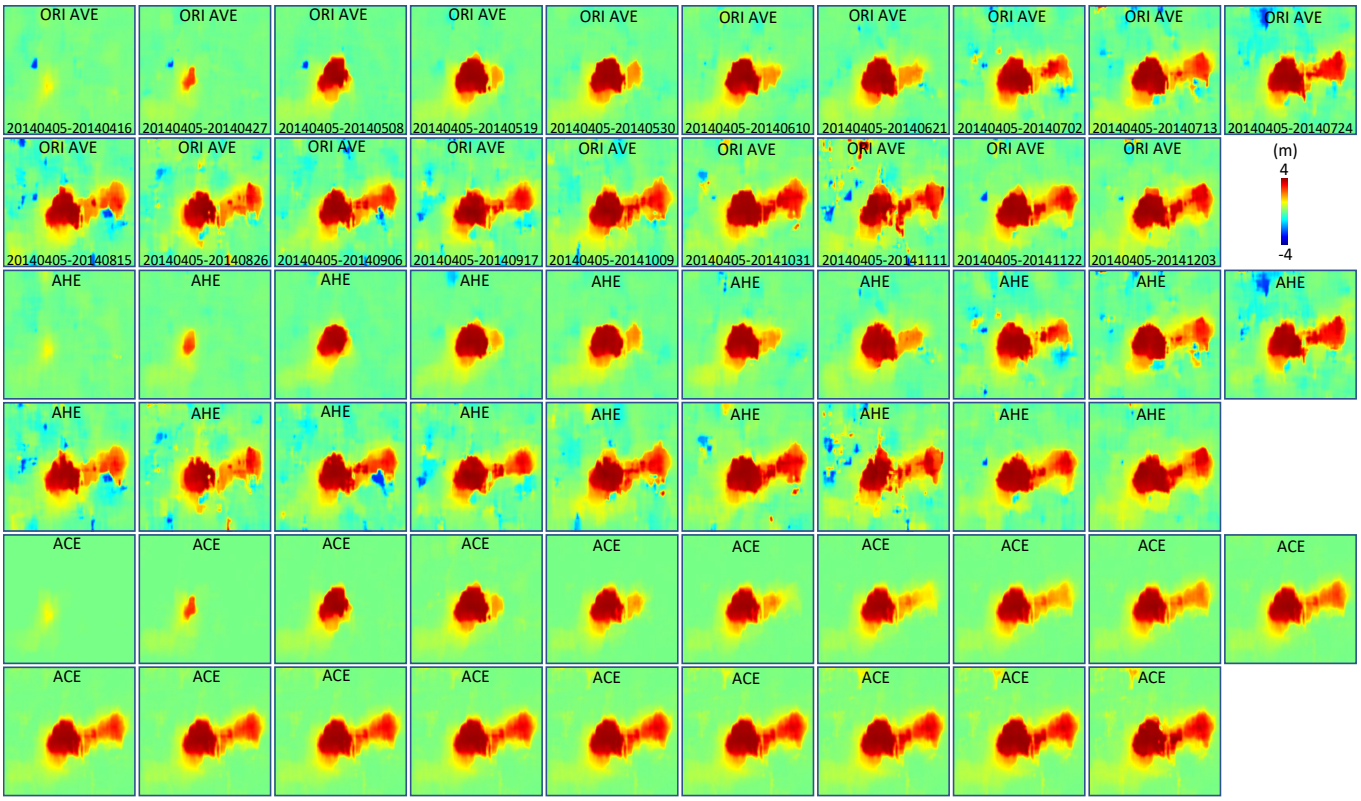

Fig. 14. Deformation time-series maps obtained from TerraSAR-X data. The first two rows are the deformation results obtained with the average image of the original HH and VV channels. The middle two rows and the last two rows are obtained with images enhanced by AHE and ACE, respectively.

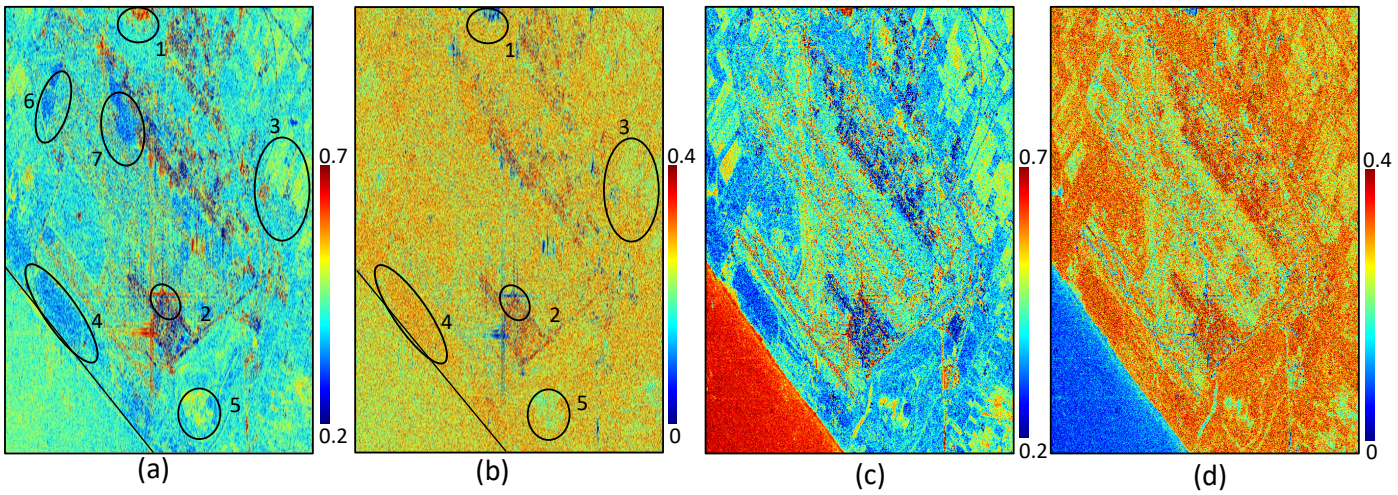

Fig. 15. (a) and (b) are r_1 and r_3, respectively, obtained with Sentinel-1 $\{VV, HV\}$ dual pol data. (c) and (d) are r_1 and r_3, respectively, obtained with Radarsat-2 $\{VV, HV\}$ dual pol data.

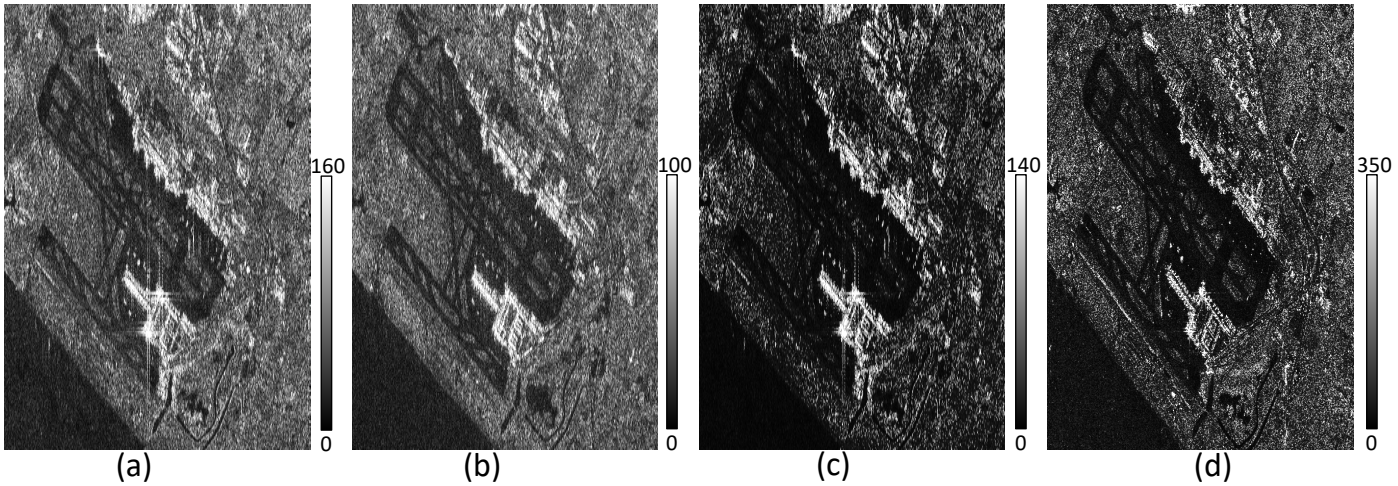

Fig. 16. Amplitude comparison before and after the application of ACE. (a) is the original VV Sentinel-1 image, (b) is the original HV Sentinel-1 image, (c) is the ACE enhanced Sentinel-1 image, and (d) is the Radarsat-2 image enhanced by ACE with $\{VV, HV\}$ polarizaton.

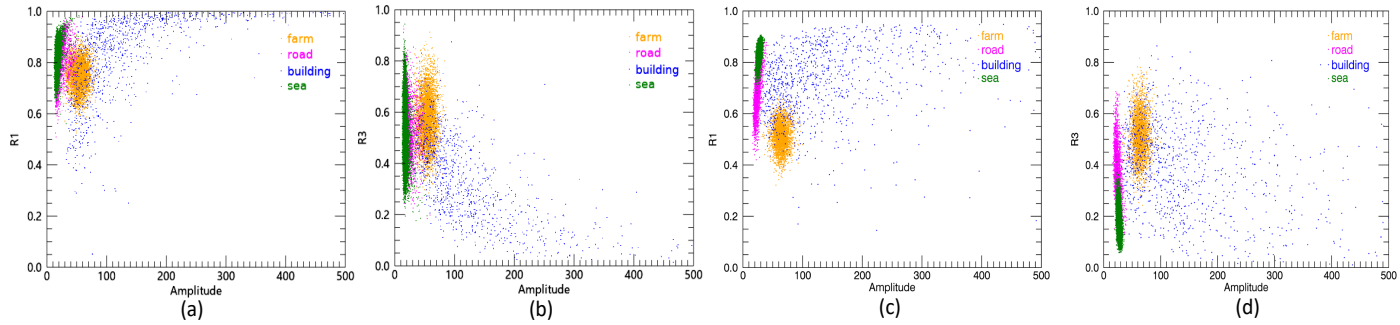

Fig. 17. Scatter plots of similarity parameters vs amplitude for different categories of ground features and sensors. Sentinel-1 $\{VV, HV\}$ data: (a) r_1 and (b) r_3 scatter plots. Radarsat-2 $\{VV, HV\}$ data: (c) r_1 and (d) r_3 scatter plots.

values. Some inconsistences appear. The low reflectivity areas in black circles 6 and 7 are not observed in Fig.15 (c), but they appear in Fig.3(b). Results from quad-pol data are more reliable than dual-pol, which means the r_1 values in black circles 6 and 7 obtained with Sentinel-1 are more accurate than results in Fig.15 (c), although they are calculated from the same polarization channels. On the other side, the runways are more obscure, the difference between sea area and lands are smaller. From amplitude images in Fig.16 it can be seen that Sentinel-1 images are noisier in the sea area than Radarsat-2, a lot of speckle noise, while the same area in Radarsat-2 images is clear. This speckle noise also has influence on r_3. Most details disappear, although blur similarities can be seen with black circles in Fig. 15(b). The comparison with the same polarization channels but different sensors shows the uncertainty of the similarity parameters from dual-pol data.

The amplitude images of original Sentinel-1 VV and HV channels, the ACE enhanced Sentinel-1 and Radarsat-2 amplitude images are shown in Fig.16. It can be seen that after ACE, the contrast is improved. And the enhanced images shown in (c) and (d) are very similar, while Radarsat-2 image has more details because its resolution is better. The blurring in the azimuth direction in Sentinel-1 images is due to its worst resolution in this direction, $22m$ compared with $5.1m$ of Radarsat-2.

Fig.17 shows the scatter plots of the similarity parameters versus amplitude obtained with Sentinel-1 and Radarsat-2 data. Four ground features are chosen in the same locations as in Fig.4. It can be seen that the similarity parameters of different features from Sentinel-1 data do not allow a good discrimination. The different features can only be distinguished by amplitude. The discrimination from Radarsat-2 data is better, but not as good as with quad-pol data. For buildings, relationship between similarity parameters and amplitude seems to be more noticeable from Sentinel-1 data than from Radarsat-2 data.

The differences in the results between Sentinel-1 and Radarsat-2 data can be mainly associated to the differences in the resolution: around 5.0×5.0 m for Radarsat-2 and 3.2×22.0 m for Sentinel-1. Low-resolution pixels then to increase speckle and mix the polarimetric features making more difficult its separation and categorization [21].

V. Discussion

The proposed ACE-OT can improve the OT performance by the images contrast enhancement. The enhancement performance mainly depends on the capacity to separate the different scattering mechanisms. Since the current satellite SAR sensors can have up to four different polarization combinations (quad-pol $\{HH, VV, VH, HV\}$ and different dual-pol combinations, $\{HH, VH\}$, $\{VV, HV\}$ or $\{HH, VV\}$), it is necessary to compare their performance and evaluate the limitations of the dual-pol cases when extracting the similarity parameters. The 31 quad-pol Radarsat-2 images mentioned in Section III are used to simulate the different dual-pol combinations.

Fig. 18 shows the reflection mechanisms obtained considering only co-pol data, $\{HH, VV\}$. From Eq. (5), (6), (18) and (19) it can be found that the HH and VV data can distinguish single and double bounce effectively. However, due to the lack of cross-pol data, r_1 and r_2 are larger than those obtained by quad-pol data. The entropy obtained by the co-pol data has the same trend as the one obtained by the quad-pol data, the runways and bare land have low entropy values, while the buildings and land with vegetation have high entropy values. However, the lack of cross-pol data causes that many details are lost. For example, all boundaries become blurred and the lanes disappear. In addition, the entropy values in the black circles 1-4 in Fig. 18 (c) are inconsistent with those from quad-pol data in Fig. 3. On the top of the black rectangle 5 and in the center of the black rectangles 6-7 in Fig. 18 (d), the entropy values obtained by quad-pol data are lower than those of its surroundings but it is just the opposite with $HH - VV$ data. For quad-pol data, in the black rectangle 8 there is bare land, that has low entropy values, that is surrounded by a vegetated area, with high entropy values. On the contrary, the results with dual-pol data of rectangle 4 show almost pure noise. These indicate that the lack of co-pol data not only causes a loss of details in the entropy map but also erroneous results.

Fig. 19 shows the scatter mechanisms obtained by $\{HH, VH\}$ dual-pol data according to Eq. (25) and (26). It can be seen that the obtained single bounce contributions in Figure 19 (a) are similar to the results obtained with quad-pol data, but the values of r_1 obtained by cross-pol data are smaller. For a small part of the farmlands (in the black circles 1, 2), the roads (in the black circle 4), and the parking lot (in the black circle 5), they have large r_1 values. But according to Fig. 3, quad-pol data shows that single bounce is weak and double bounce strong, which indicates that the $\{HH, VH\}$ data cannot effectively distinguish between single and double bounce in these areas. Besides, in other areas r_1 values obtained by $\{HH, VH\}$ are inconsistent with r_1 values from $\{VV, HV\}$ in Fig. 15(c). For example, in the black circle 3 in Fig. 19(a), the road has a higher single reflection value than in Fig. 15 (c). This means that in these dual-pol combinations, the information of phase between the two channels cannot be unambiguously associated with scattering mechanisms. In other words, we measure the reflected wave features (which depend on the incident polarisation), not the target features [38].

The entropy obtained from $\{HH, VH\}$ or $\{VV, HV\}$ data is similar to the one obtained by the quad-pol case, but some details are lost, and the values of r_3 obtained by cross-pol data are larger. For example, the boundary between the cement pavement and the aircraft runway in the black circle 6 is blurred, but it is perfectly clear in Fig. 3 (d).

The histograms of the optimized contrast for the four different polarization combinations plus HH are shown in Fig. 20. The contrast is calculated with Eq. (15) using a 3×3 moving averaging window. As it can be seen in Fig. 20, the initial image contrast represented by HH can be improved with the use of polarimetric data. The largest improvement is achieved with quad-pol data, followed by the dual-pol data with co-polar channels and finally the dual-pol with one co-polar and one cross-polar channels, almost with identical performance.

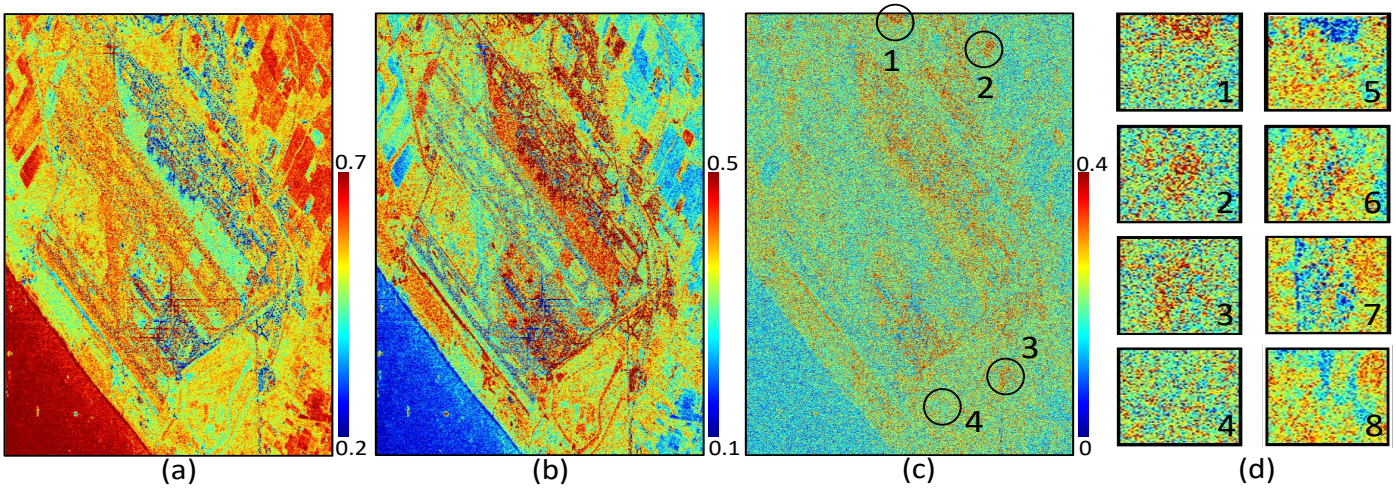

Fig. 18. Scatter mechanism maps obtained from the temporally averaged Radarsat-2 dual co-polar data, $\{HH, VV\}$. (a), (b) and (c) are the values of similarity parameters r_1, r_2 and r_3. The zoom of the areas encircled in black are shown in the rectangles labelled 1 to 4 in (d), 5-8 are the same areas shown in Fig. 3 (d) as references.

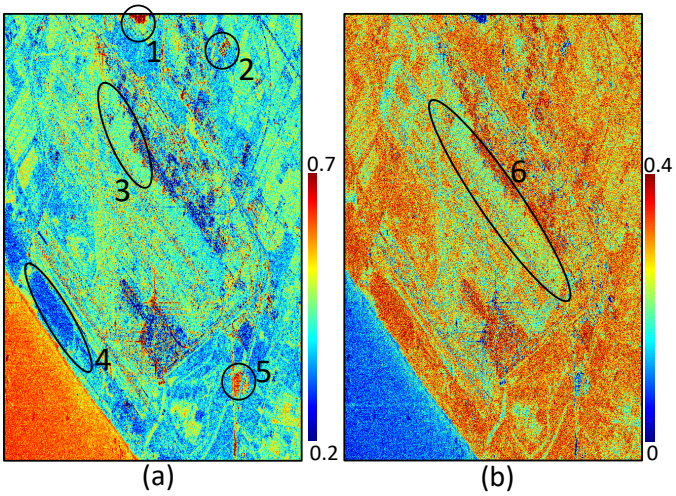

Fig. 19. Scatter mechanism maps obtained from the temporally averaged Radarsat-2 dual cross-pol data, $\{HH, VH\}$. (a) and (b) are the values of similarity parameters r_1 and r_3.

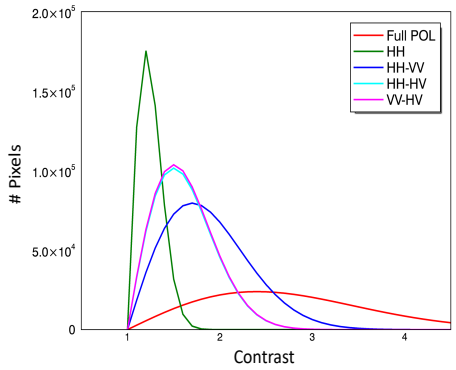

Fig. 20. Histograms of the ACE contrast enhancement using different combinations of polarimetric channels.

Dual-pol with co-polar channels allows to better determine the reflection properties than the other dual-pol cases. Overall, the single reflection and double bounce obtained by two co-polar data are accurate. Although the entropy is unsatisfactory, it does not participate in the contrast enhancement procedure.

VI. Conclusion

An Amplitude Contrast Enhancement method (ACE) taking advantage of polarimetric diversity is proposed in this paper to improve the performance of the images cross-correlation based Offset Tracking (OT) deformation estimation. This method, which is inspired by [23], looks for the best combination of polarimetric reflection mechanisms to achieve the highest amplitude contrast in the images.

Three SAR data sets, one with 31 quad-pol Radarsat-2 images, another with 32 dual-pol Sentinel-1 images, and the last with 20 dual-pol Terrasar-X images, have been used to evaluate the performance of the proposed method. The first two datasets have been acquired over the Barcelona airport (Spain) while the third one over a mountainous mining area in Daliuta (China).

As benchmark, ACE has been compared with another contrast enhancement method. Among the different methods, the Adaptive Histogram Enhancement (AHE) has been selected as it works locally, which makes it comparable to ACE that does the same. The results show that the simulated offset added to the airport images can be better retrieved with ACE than with AHE. The former considers the scattering characteristics of the pixels when improving the contrast while the latter treats the data as a simple black and white image. The comparison of the original and retrieved deformation time-series has demonstrated the positive impact of the proposed contrast enhancement method in the performance of OT. Similarly, the large deformations caused by the coal mining activity in the mountainous area of Daliuta have been better obtained with ACE than with the original averaged polarimetric channels or AHE. The results have shown that subsidence values have

reached values of almost 4 m in only 33 days. The comparison of the error maps for the three approaches indicates that ACE is able to provide more consistent results. Although the three methods are quite able to estimate the shape of the deformation bowl and their values, the results with the original images and AHE show non-consistent deformations throughout the deformation map. Non-consistent results mean deformations that appear in a particular time interval but disappear in the next one, which obviously are not realistic.

The enhancing performances of the different polarization combinations, quad- and dual-pol, are discussed and analyzed. Firstly, the accuracy of the scatter mechanism extraction is validated. Among all dual-pol cases, $\{HH, VV\}$ combination presents the best performance obtaining the single and double reflections. The other dual-pol combinations, one co-polar and one cross-polar, can be quite inaccurate in some areas. Secondly, the performances among the different polarization combinations are then compared. As expected, quad-pol data achieves the highest contrast optimization. The performances of the combinations of one co-pol and one cross-pol data, $\{XX, YX\}$, are almost identical and clearly inferior to the combination of the two co-polar data, $\{HH, VV\}$. Sentinel-1 polarization data is tested and the results are quite similar with those using the same polarization combination from Radarsat-2 data. Differences in the retrieved similarity parameters are mostly due to the worst resolution of Sentinel-1, which tends to rise the speckle and mix the different scattering mechanisms present in the resolution cell when compared with Radarsat-1. In any case, dual-pol data allows also to enhance the contrast of the images and, as a consequence, reduce the presence of non-consistent results in the deformation maps.

ACKNOWLEDGMENT

Radarsat-2 images were provided by MDA in the framework of the scientific project SOAR-EU 6779. TerraSAR-X images have been provided by the German Aerospace Center (DLR) in the framework of Project GEO0389 of the TerraSAR-X scientific program. Sentinel-1 data has been provide by ESA. DEMs were from the Instituto Geografico Nacional (IGN) of Spain and NASA/JPL. Some figures were prepared using the public domain GMT software (Wessel and Smith, 1998). Optical images provided by GoogleEarth.

REFERENCES

[1] E. Erten, "Glacier velocity estimation by means of a polarimetric similarity measure," *IEEE Transactions on Geoscience and Remote Sensing*, vol. 51, no. 6, pp. 3319–3327, 2013.

[2] H. Fan, X. Gao, J. Yang, K. Deng, and Y. Yu, "Monitoring mining subsidence using a combination of phase-stacking and offset-tracking methods," *Remote Sensing*, vol. 7, no. 7, pp. 9166–9183, 2015.

[3] C. Wang, X. Mao, and Q. Wang, "Landslide displacement monitoring by a fully polarimetric SAR offset tracking method," *Remote Sensing*, vol. 8, no. 8, p. 624, 2016.

[4] S.-H. Yun, H. Zebker, P. Segall, A. Hooper, and M. Poland, "Interferogram formation in the presence of complex and large deformation," *Geophysical Research Letters*, vol. 34, no. 12, 2007.

[5] V. D. Navarro-Sanchez, J. M. Lopez-Sanchez, and F. Vicente-Guijalba, "A contribution of polarimetry to satellite differential SAR interferometry: Increasing the number of pixel candidates," *IEEE Geoscience and Remote Sensing Letters*, vol. 7, no. 2, pp. 276–280, 2009.

[6] V. D. Navarro-Sanchez, J. M. Lopez-Sanchez, and L. Ferro-Famil, "Polarimetric approaches for persistent scatterers interferometry," *IEEE Transactions on Geoscience and Remote Sensing*, vol. 52, no. 3, pp. 1667–1676, 2013.

[7] R. Iglesias, D. Monells, X. Fabregas, J. J. Mallorqui, A. Aguasca, and C. Lopez-Martinez, "Phase quality optimization in polarimetric differential SAR interferometry," *IEEE Transactions on Geoscience and Remote Sensing*, vol. 52, no. 5, pp. 2875–2888, 2013.

[8] B. Wu, L. Tong, Y. Chen, and L. He, "New methods in multibaseline polarimetric SAR interferometry coherence optimization," *IEEE Geoscience and Remote Sensing Letters*, vol. 12, no. 10, pp. 2016–2020, 2015.

[9] Z. Sadeghi, M. J. V. Zoej, and J.-P. Muller, "Monitoring land subsidence in a rural area using a combination of ADInSAR and polarimetric coherence optimization," *IEEE Journal of Selected Topics in Applied Earth Observations and Remote Sensing*, vol. 10, no. 8, pp. 3582–3590, 2017.

[10] M. Esmaeili and M. Motagh, "Improved Persistent Scatterer analysis using Amplitude Dispersion Index optimization of dual polarimetry data," *ISPRS Journal of Photogrammetry and Remote Sensing*, vol. 117, pp. 108–114, 2016.

[11] M. Esmaeili, M. Motagh, and A. Hooper, "Application of dual-polarimetry SAR images in multitemporal InSAR processing," *IEEE Geoscience and Remote Sensing Letters*, vol. 14, no. 9, pp. 1489–1493, 2017.

[12] K. Ishitsuka, T. Matsuoka, and M. Tamura, "Persistent scatterer selection incorporating polarimetric SAR interferograms based on maximum likelihood theory," *IEEE Transactions on Geoscience and Remote Sensing*, vol. 55, no. 1, pp. 38–50, 2016.

[13] A. G. Mullissa, V. Tolpekin, A. Stein, and D. Perissin, "Polarimetric differential SAR interferometry in an arid natural environment," *International Journal of Applied Earth Observation and Geoinformation*, vol. 59, pp. 9–18, 2017.

[14] A. G. Mullissa, D. Perissin, V. A. Tolpekin, and A. Stein, "Polarimetry-based distributed scatterer processing method for PSI applications," *IEEE Transactions on Geoscience and Remote Sensing*, vol. 56, no. 6, pp. 3371–3382, 2018.

[15] Z. Sadeghi, M. J. V. Zoej, and J.-P. Muller, "Combination of persistent scatterer interferometry and single-baseline polarimetric coherence optimisation to estimate deformation rates with application to tehran basin," *PFG–Journal of Photogrammetry, Remote Sensing and Geoinformation Science*, vol. 85, no. 5, pp. 327–340, 2017.

[16] F. Zhao and J. J. Mallorqui, "Coherency matrix decomposition-based polarimetric persistent scatterer interferometry," *IEEE Transactions on Geoscience and Remote Sensing*, vol. 57, no. 10, pp. 7819–7831, 2019.

[17] ——, "SMF-POLOPT: An adaptive multitemporal pol (DIn) SAR filtering and phase optimization algorithm for PSI applications," *IEEE Transactions on Geoscience and Remote Sensing*, vol. 57, no. 9, pp. 7135–7147, 2019.

[18] R. Iglesias González, A. Aguasca Solé, F. J. Fabregas Canovas, J. J. Mallorquí Franquet, D. Monells Miralles, C. López Martínez, and L. Pipia, "Ground-based polarimetric SAR interferometry for the monitoring of terrain displacement phenomena-part II: applications," *IEEE Journal of Selected Topics in Applied Earth Observations and Remote Sensing*, vol. 8, no. 3, pp. 994–1007, 2015.

[19] L. Pipia, X. Fabregas, A. Aguasca, C. Lopez-Martinez, S. Duque, J. J. Mallorqui, and J. Marturia, "Polarimetric differential SAR interferometry: First results with ground-based measurements," *IEEE Geoscience and Remote Sensing Letters*, vol. 6, no. 1, pp. 167–171, 2008.

[20] C. López-Martínez, X. Fàbregas, and L. Pipía, "PolSAR and PolInSAR model based information estimation," in *2009 IEEE International Geoscience and Remote Sensing Symposium*, vol. 3. IEEE, 2009, pp. III–959.

[21] F. Zhao, J. J. Mallorqui, and J. M. Lopez-Sanchez, "Impact of SAR Image Resolution on Polarimetric Persistent Scatterer Interferometry With Amplitude Dispersion Optimization," *IEEE Transactions on Geoscience and Remote Sensing*, 2021.

[22] F. Zhao, T. Wang, L. Zhang, H. Feng, S. Yan, H. Fan, D. Xu, and Y. Wang, "Polarimetric Persistent Scatterer Interferometry for Ground Deformation Monitoring with VV-VH Sentinel-1 Data," *Remote Sensing*, vol. 14, no. 2, p. 309, 2022.

[23] J. Yang, G. Dong, Y. Peng, Y. Yamaguchi, and H. Yamada, "Generalized optimization of polarimetric contrast enhancement," *IEEE Geoscience and Remote Sensing Letters*, vol. 1, no. 3, pp. 171–174, 2004.

[24] J. Yang, Y.-N. Peng, and S.-M. Lin, "Similarity between two scattering matrices," *Electronics Letters*, vol. 37, no. 3, pp. 193–194, 2001.

[25] W. Boerner, H. Brand, L. Cram, D. Giessing, and A. Jordan, "Inverse methods in electromagnetic imaging; Proceedings of the NATO Advanced Research Workshop, Bad Windsheim, West Germany, September 18-24, 1983. Parts 1 & 2," *Inverse Methods in Electromagnetic Imaging*, 1985.
[26] W.-M. Boerner, L. A. Cram, W. A. Holm, D. E. Stein, W. Wiesbeck, W. Keydel, D. Giuli, D. T. Gjessing, F. A. Molinet, and H. Brand, *Direct and inverse methods in radar polarimetry*. Springer Science & Business Media, 2013, vol. 350.
[27] W.-M. Boerner, "Introduction to radar polarimetry–with assessments of the historical development and of the current State-of-the-Art," *Electromagnetic Wave Interactions*, pp. 139–214, 1996.
[28] A. Kostinski and W. Boerner, "On the polarimetric contrast optimization," *IEEE Transactions on Antennas and Propagation*, vol. 35, no. 8, pp. 988–991, 1987.
[29] J. Huynen, "Phenomenological theory of radar targets," Ph.D. dissertation, Technical University of Delft, 1970.
[30] S. R. Cloude and E. Pottier, "An entropy based classification scheme for land applications of polarimetric SAR," *IEEE Transactions on Geoscience and Remote Sensing*, vol. 35, no. 1, pp. 68–78, 1997.
[31] A. Swartz, H. Yueh, J. Kong, L. Novak, and R. Shin, "Optimal polarizations for achieving maximum contrast in radar images," *Journal of Geophysical Research: Solid Earth*, vol. 93, no. B12, pp. 15 252–15 260, 1988.
[32] H. Mott and W.-M. Boerner, "Polarimetric contrast enhancement coefficients for perfecting highresolution POL-SAR/SAL image feature extraction," in *Wideband Interferometric Sensing and Imaging Polarimetry*, vol. 3120. International Society for Optics and Photonics, 1997, pp. 106–117.
[33] I. G. Cumming and F. H. Wong, "Digital processing of synthetic aperture radar data," *Artech House*, vol. 1, no. 3, 2005.
[34] M. R. Hestenes, E. Stiefel *et al.*, *Methods of conjugate gradients for solving linear systems*. NBS Washington, DC, 1952, vol. 49, no. 1.
[35] E. Sansosti, P. Berardino, M. Manunta, F. Serafino, and G. Fornaro, "Geometrical SAR image registration," *IEEE Transactions on Geoscience and Remote Sensing*, vol. 44, no. 10, pp. 2861–2870, 2006.
[36] S. M. Pizer, E. P. Amburn, J. D. Austin, R. Cromartie, A. Geselowitz, T. Greer, B. ter Haar Romeny, J. B. Zimmerman, and K. Zuiderveld, "Adaptive histogram equalization and its variations," *Computer Vision, Graphics, and Image Processing*, vol. 39, no. 3, pp. 355–368, 1987.
[37] C. Werner, U. Wegmuller, T. Strozzi, and A. Wiesmann, "Precision estimation of local offsets between pairs of SAR SLCs and detected SAR images," in *International Geoscience and Remote Sensing Symposium*, vol. 7, 2005, p. 4803.
[38] L. Mascolo, S. R. Cloude, and J. M. Lopez-Sanchez, "Model-based decomposition of dual-pol SAR data: application to Sentinel-1," *IEEE Transactions on Geoscience and Remote Sensing*, vol. 60, pp. 1–19, 2022.

Sen Du received the B.S. degrees in geodesy and surveying engineering from China University of Mining and Technology, Xuzhou, China, in 2015. He is currently working toward the Ph.D. degree at the Universitat Politècnica de Catalunya, Barcelona, Spain.

He joined the CommSensLab, Universitat Politècnica de Catalunya, in September 2018, where his main work focuses on application of SAR to terrain deformation monitoring with orbital and ground data. His research interests include SAR interferometry and offset tracking techniques and its application on terrain deformation detection.

Jordi J. Mallorqui (S'93-M'96-SM'13) was born in Tarragona, Spain, in 1966. He received the Ingeniero and Doctor Ingeniero degrees in telecommunications engineering from the Universitat Politècnica de Catalunya (UPC), Barcelona, Spain, in 1990 and 1995, respectively.

Since 1993, he has been teaching with the School of Telecommunications Engineering of Barcelona, UPC, first as an Assistant Professor, later in 1997 as an Associate Professor, and since 2011 as a Full Professor. His teaching activity involves microwaves, radionavigation systems, and remote sensing. He spent a sabbatical year with the Jet Propulsion Laboratory, Pasadena, CA, USA, in 1999, working on interferometric airborne synthetic aperture radar (SAR) calibration algorithms. He is currently working on the application of SAR interferometry to terrain-deformation monitoring with orbital, airborne, and ground data; vessel detection and classification from SAR images; and 3-D electromagnetic (EM) simulation of SAR systems. He has published more than 100 papers on microwave tomography, EM numerical simulation, and SAR processing, interferometry, and differential interferometry in refereed journals and international symposia.

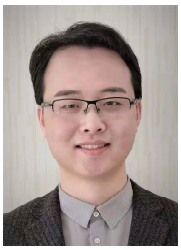

Feng Zhao (S'17-M'20) received the M.S. degree from the China University of Mining and Technology (CUMT), Xuzhou, China, in June 2016 and the Ph.D. degree from the Universitat Politècnica de Catalunya, Barcelona, Spain, in September 2019.

Since November 2019, he has been with the School of Environment Science and Spatial Informatics, CUMT, and with the Key Laboratory of Land Environment and Disaster Monitoring of the Ministry of Natural Resources of China, as a assistant professor. His main work focuses on the development of advanced pixel selection and optimization algorithms for multi-temporal (Pol)DInSAR techniques. His research interests include advanced multi-temporal InSAR techniques and its application on terrain deformation detection.